

pubs.acs.org/JPCB Article

Modeling Amyloid Aggregation Kinetics: A Case Study with Sup35NM

Aditi Sharma, Matthew A. McDonald, Harrison B. Rose, Yury O. Chernoff, Sven H. Behrens, and Andreas S. Bommarius*



Cite This: https://doi.org/10.1021/acs.jpcb.0c11250



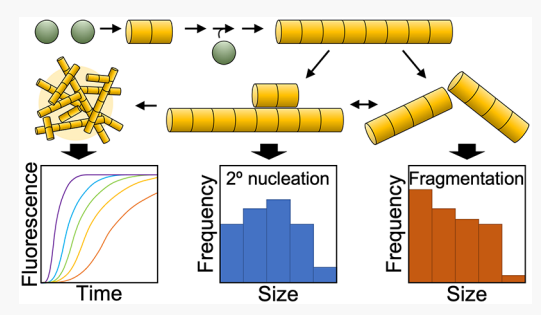
ACCESS

Metrics & More

Article Recommendations

Supporting Information

ABSTRACT: Understanding the aggregation mechanism of amyloid proteins, such as Sup35NM, is essential to understanding amyloid diseases. Significant recent work has focused on using the fluorescence of thioflavin T (ThT), which undergoes a red shift when bound to amyloid aggregates, to monitor amyloid fibril formation. In the present study, the progression of the total mass of aggregates during fibril formation is monitored for initial monomer concentrations in order to infer the relevant aggregation mechanisms. This workflow was implemented using the amyloid-forming fragment Sup35NM under different agitation conditions and for initial monomer concentrations spanning 2 orders of magnitude. The analysis suggests that primary nucleation, monomeric elongation, secondary nucleation, and fragmentation might all be



relevant, but their relative importance could not be determined unambiguously, despite the large set of high-quality data. Discriminating between the fibril-generating processes is shown to require additional information, such as a fibril length distribution. Using Sup35NM as a case study, a framework for fitting the parameters of arbitrary amyloid aggregation kinetics is developed based on a population balance model (PBM), which resolves not only the total aggregate mass (monitored experimentally via ThT fluorescence) but the entire fibril length distribution over time. In addition to the rich new set of ThT fluorescence data, we have reanalyzed a previously published aggregate size distribution using this method. With the size distribution, it was determined that in the reanalyzed *in vitro* experiment, secondary nucleation generated significantly fewer new Sup35NM fibrils than fragmentation. The proposed strategy of applying the same PBM to a combination of kinetic data from fluorescence monitoring and experimental fibril length distributions will allow the inference of aggregation mechanisms with far greater confidence than fluorescence studies alone.

■ INTRODUCTION

Amyloids are fibrous, self-seeding cross- β aggregates of misfolded proteins that have drawn much attention because of their association with a number of important neurodegenerative disorders such as Parkinson's and Alzheimer's disease.^{2,3} Infectious amyloids called prions can transmit the amyloid state between organisms and have been implicated in transmissible spongiform encephalopathies, such as sheep scrapie, mad cow disease, and human Creutzfeldt-Jakob disease. Spontaneous formation of amyloids in protein- or peptide-based drug preparations can reduce drug efficacy and raise the risk of unwanted immunogenicity.⁴ Amyloid-based prions manifest themselves as cytoplasmically heritable elements controlling phenotypic traits in fungi; such fungal (especially yeast) prions serve as popular models for fundamental studies of amyloid aggregation and transmission.5,6

The process by which the native protein converts into filamentous amyloid aggregates is believed to follow at least two fundamental steps: a nucleation step, in which proteins undergo a spontaneous transition in their secondary structure toward a β -sheet-rich conformation and aggregate into an

initial nucleus, and an elongation step, in which existing aggregates of at least the critical nucleus size induce a newly immobilized protein monomer to undergo the same conformational change and join the growing aggregate in analogy to one-dimensional crystallization. Some authors argue that nucleation is a multistep process, including both aggregation and conformational rearrangement; however, further dissection of the primary nucleation process is beyond the scope of the present work. Experimental studies of the associated kinetics commonly use fluorescence probes to monitor the total fibril mass over time.

It has been recognized, however, that the number of aggregates present can also be influenced significantly by secondary processes such as fragmentation (producing new growing fibril ends) and fibril-catalyzed secondary nucleation

Received: December 17, 2020 Revised: April 1, 2021



Figure 1. Processes involved in amyloid formation and proliferation. Monomers (spheres) aggregate into fibrils (cylinders). Primary processes on the left and secondary fibril-generating mechanisms on the right.

(promoting formation of new nuclei rather than immobilizing protein molecules into growing fibrils) (Figure 1). $^{10-14}$ Recent models for analytical solutions to the kinetic equations have incorporated these processes as well. $^{15-18}$ It has been argued that an even more detailed picture of the mechanisms at work in amyloid aggregation can be obtained from global fits to high quality experimental aggregation data for multiple protein concentrations. 18,19 Particular attention has been given to the spread of kinetic curves with protein concentration expressed as the scaling parameter γ

$$\gamma = \frac{d(\ln t_{50})}{d(\ln m_0)} \tag{1}$$

where t_{50} is the time to reach 50% of the maximum fluorescence recorded and m_0 is the initial monomer concentration. The value of this parameter, along with any systematic variation along the concentration coordinate, has been proposed to hold the key for identifying the aggregation mechanisms at work. ^{15,16,20,21}

The rate equations associated with (primary and secondary) nucleation, elongation, and fragmentation lead to a partial differential equation describing the evolution of the aggregate size distribution. A popular simpler approach considers only the total aggregate number and mass, that is, the first two moments of the fibril length distribution. Their time dependence is described by a coupled nonlinear system of ordinary differential equations, for which an approximate analytical solution is available. 13 Global fits of this type of model to sets of experimental kinetic data have been used successfully to deduce mechanistic differences in the aggregation of A β 40 and A β 42, the two common forms of the amyloid beta-peptide forming the plaques associated with Alzheimer's disease,²² and fueled the hope that the same strategy will provide similarly conclusive evidence of the aggregation mechanisms at work in other amyloid systems. In this spirit, the free online platform AmyloFit, developed by Knowles and co-workers, 18 allows users to upload their own sets of experimental kinetic curves and carry out the global fits to determine "what kind of microscopic processes are dominant and determine the aggregation kinetics of their protein system."

In the present study, we use a full population balance model (PBM) to analyze a large set of kinetic data for the amyloid formation of Sup35NM, a fragment of the yeast protein Sup35p that contains a prion-forming domain and is routinely employed as a model for studying major parameters of amyloid aggregation *in vitro*. Our group previously has demonstrated the influence of ionic composition of the solution on the aggregation kinetics of Sup35NM 1,23 and also has reported the differences in effects of ions on amyloid aggregation by Sup35NM and $A\beta42$. Our analysis of the full aggregate size distribution and comparison with results from the AmyloFit analysis show that even global fits for peptide concentrations

spanning 2 orders of magnitude do not allow us to unambiguously identify the dominant aggregation mechanism.

MATERIALS AND METHODS

Plasmid constructs containing the Sup35NM coding region of the *Saccharomyces cerevisiae SUP35* gene with a C-terminal hexahistidine (His6) tag were expressed in the *Escherichia coli* host strain HMS174 (DE3) pLysS (Novagen) to produce the Sup35NM-(His6) proteins, and purification was carried out as described previously. ^{23,25} Briefly, the cells were transformed with the cloning vector, protein expression was induced using isopropyl β -D-1-thiogalactopyranoside (IPTG) at 37 °C, and

Expression and Purification of Sup35NM-(His6).

the cells were harvested about 4 h after induction. The cell pellets were stored at $-80~^{\circ}\mathrm{C}$ until purification, and the protein was purified by Ni-NTA His-tag affinity purification under denaturing conditions. The purified protein was precipitated using cold methanol at $-20~^{\circ}\mathrm{C}$ and the protein pellet was collected by centrifugation and washed with cold methanol and finally stored at $-80~^{\circ}\mathrm{C}$ in 80% methanol.

Fibrillation Assays Using Thioflavin T. Protein pellets stored at -80 °C were collected by centrifugation. The supernatant was discarded and the protein was resuspended in 8 M urea. Sup35NM was then concentrated by 10 kDa centrifugal filtration and diluted 100-fold with PBS buffer at pH 7.4. The samples were boiled for about 10 min to break down any preformed aggregates before starting the aggregation experiments. 1 mM thioflavin T (ThT; Sigma-Aldrich) solution was prepared fresh in PBS buffer. Five replicates of each aggregation experiment were conducted in a clear flatbottom 96-well plate (Greiner CELLSTAR) with the final ThT concentration of 100 µM and Sup35NM at initial concentrations (m_0) 0.125, 0.25, 0.5, 0.75, 1, 2.5, 5 7.5 10, 15, 20, 25, and 30 μ M in PBS at 37 °C. A BioTek Synergy H4 Hybrid multi-mode microplate reader (Winooski, VT) was used to provide linear shaking, with an amplitude of 5 mm at three different rates, 0, 17, and 19 min⁻¹, referred to as no shaking, slow shaking, and fast shaking, respectively. Fluorescence readings were taken every 10 min for 5 days using an excitation wavelength of 440 nm and an emission wavelength of 485 nm. They are interpreted as a measure of the total amount of amyloid aggregates formed. 26,27 Five repetitions of each condition were performed, and each was independently baselined and the results fit individually, as averaging sigmoids with different stochastic lag times introduce artificial features.²⁸

The correlation between aggregate mass concentration, *a*, and ThT fluorescence, *f*, is best described as a piecewise linear function, where at low aggregate mass concentration, the proportionality constant is about fourfold greater than at high aggregate mass concentration (Figure 2). Here, mass concentration (measured in moles of aggregated monomer per liter) is used to differentiate from other concentrations such as number concentration (number of aggregates per

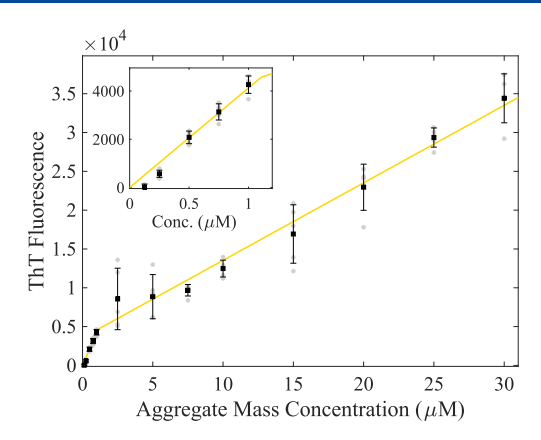


Figure 2. Calibration curve used to correlate aggregate mass concentration and ThT fluorescence. The inset shows the low concentration regime a $\leq 1.1~\mu M$.

liter). The transition point between the high and low concentration regimes is approximately 1.1 μ M.

$$f = \begin{cases} 4120a & a \le 1.1\\ 1000a + 3520 & a > 1.1 \end{cases} \tag{2}$$

Population Balance Modeling. A PBM is used to integrate the various kinetic phenomena (in this study elongation, primary nucleation, secondary nucleation, and fragmentation) into an overall model representing the evolution of the fibrils of different lengths over time. The PBM is formalized in eqs 3 and 4

$$\frac{\partial A(L, t)}{\partial t} + E(t) \frac{\partial A(L, t)}{\partial L}
= -FA(L, t) + F \int_{L}^{\infty} b(L, \lambda) A(\lambda, t) d\lambda$$
(3)

where the population density function, A, is a function of fibril length and time and the elongation rate, E, and the fragmentation rate, F, are both independent of length. Elongation and nucleation (see below) are the product of rate constants and time-varying free monomer concentrations. More details on fragmentation are given in the discussion, but briefly, the first term on the right side of eq 3 accounts for the fibrils destroyed by fragmentation and the integral term accounts for the new fibrils generated during fragmentation; b describes the distribution of fragment sizes. The boundary conditions are

$$A(L, t = 0) = 0$$

$$A(L = L_{N}, t > 0) = \frac{N(t)}{E(t)}$$
(4)

where $L_{\rm N}$ is the size of a nucleus, N refers to the nucleation rate, and E refers to the elongation rate, as previously indicated. For the temporal boundary condition, no fibrils are present at the start of the experiment as no seeded experiments were conducted. For the spatial boundary condition, it is assumed that $L_{\rm N}=2$, that is, a nucleus consists of two aggregated monomers; however, this boundary condition holds for all values of $L_{\rm N}$, provided the total mass of critical nuclei remains negligible compared to the total mass of all aggregates.

In previous studies, the population density function has been reduced to its first two principal moments, P and M, which can be computed from A by

$$P(t) = \int_{L_{N}}^{\infty} A(\lambda, t) d\lambda$$

$$M(t) = \int_{L_{N}}^{\infty} \lambda A(\lambda, t) d\lambda$$
(5)

Assuming that the aggregates are approximately one-dimensional and that elongation only occurs at fibril ends, M = a, the mass concentration (M will be used to represent mass concentrations calculated from A and a represents experimentally measured values). The second moment can then be used to calculate a mass balance, shown in eq 6, giving a fully specified system of differential equations

$$m_0 = m + M \tag{6}$$

where m_0 is the initial monomer concentration and m is the instantaneous free-monomer concentration.

The PBM was solved with the method of lines, whereby the spatial dimension was discretized, giving the evolution of aggregate sizes over time. The resulting system of ODEs was solved with the 4th order Runge-Kutta MATLAB ODE-solver ode45. Kinetic parameters, θ , were fit by iteratively solving the PBM and least squares regression according to

$$\min_{\theta} \sum_{i} \sum_{j=1}^{5} \left[\frac{1}{m_{0,i}^{2}} (M_{i}(t) - a_{ij}(t))^{2} \right]$$
(7)

where i indexes the set of initial monomer concentrations used in the fit, j represents the experiment replication number, $M_i(t)$ represents the modeled aggregate mass concentration with initial monomer concentration, and $m_{0,i}$ and a_{ij} are the measured aggregate mass concentrations with initial monomer concentration $m_{0,i}$ and repeat number j, respectively. The error is weighted by $m_{0,i}$ such that all experiments contribute equally to the fitted parameter values. The minimization was performed with the built-in MATLAB optimizer f mincon using f multiStart to ensure that the global minimum has been found. As fibril growth is approximately one-dimensional, the length is measured in monomer units; time is measured in minutes.

The primary advantage of solving A instead of P and M, which are easier to compute, is that information on aggregate sizes from experiments orthogonal to ThT fluorescence could be utilized as well. Additional information on the aggregate size distribution will be shown to be necessary to discriminate between different modes of new fibril formation.

■ RESULTS AND DISCUSSION

Sup35NM Aggregation Phenomena and Modeling. At low concentrations, a significant fraction of Sup35NM appears to persist in the monomer form. The inset in the calibration curve (Figure 2) shows that when the Sup35NM monomer is present at a concentration of 125 nM, there is no observable ThT fluorescence and therefore no detectable fibril formation, after a period of 5 days. To account for the lack of aggregation at low monomer concentrations, the phenomena of nucleation and elongation are expressed in terms of the supersaturation, σ

$$\sigma = \frac{m - m^*}{m^*} \tag{8}$$

where m^* is the saturation monomer concentration. The saturation concentration is also equivalent to the monomer concentration at which the rates of aggregation and depolymerization are equal.

Formulating elongation and nucleation in terms of supersaturation is equivalent to including an explicit rate law for depolymerization. Many studies on other amyloid peptides have successfully modeled aggregation kinetics with negligible depolymerization; ^{18,30} however, this is not possible for Sup35NM. In undersaturated solutions, aggregates may depolymerize; however, the experimental conditions probed are primarily targeted toward supersaturated conditions. In this study, the elongation rate is modeled using the following power law

$$E = k_{\rm F} \sigma^{n_{\rm E}} \tag{9}$$

where $k_{\rm E}$ and $n_{\rm E}$ are the rate constant and exponent for elongation, respectively. Two nucleation phenomena contribute to the overall nucleation rate, both modeled as power laws: primary nucleation (which occurs independently from any existing fibrils) and secondary nucleation (which occurs only when aggregates are present).

$$N = k_{N_1} \sigma^{n_1} + k_{N_2} \sigma^{n_2} M^{n_m} \tag{10}$$

Here, $k_{\rm N1}$ and $k_{\rm N2}$ are the rate constants for primary and secondary nucleation, respectively, $n_{\rm 1}$ and $n_{\rm 2}$ are the exponents with respect to supersaturation for primary and secondary nucleation, respectively, and $n_{\rm m}$ is the exponent with respect to aggregate mass concentration, applicable only to secondary nucleation.

Fragmentation is also considered as an explanation for the significant rate enhancement observed when increasing the agitation rate. The need for depolymerization to accurately model Sup35NM aggregation indicates that intermolecular bonds may not be as strong in Sup35NM as in some other amyloid proteins. The presumed weakness of these bonds could make the aggregates frangible, which agrees with the notion that Sup35 is an efficiently proliferating and highly transmissible (heritable) prion. Prion proliferation in vivo requires efficient generation of new fibrils; thus, the weakness of intermolecular bonds and ease of fragmentation could be a prerequisite for the efficient proliferation of a prion. 1,31 For this model, fragmentation, F, has a first-order dependence on aggregate mass concentration explicitly captured in the PBM eq 3, where $F = k_F$ (fragmentation rate constant) while the total rate of fragmentation is

$$F_{\text{tot}} = 1/2k_{\text{F}}M\tag{11}$$

For simplicity, it is assumed that aggregates that do fragment form two new fibrils of equal length, which results in $b(L,\lambda)=2$ if $\lambda=2L$ and b=0 otherwise. It was also assumed in the PBM formulation that fragmentation is independent of length, although this assumption is not required. Although these assumptions may oversimplify fragmentation, $a_{2,3}^{32,34,35}$ they are completely compatible with prior solutions to the amyloid aggregation problem and do not change the values of $a_{2,3}^{32,34,35}$ they are comparison with previous studies straightforward.

Secondary nucleation and fragmentation rates also depend on agitation. In this study, the parameter values characterizing these phenomena were fit at three different agitation intensities. Figure 3 shows the normalized aggregate mass concentration over time, starting from 10 μ M Sup35NM

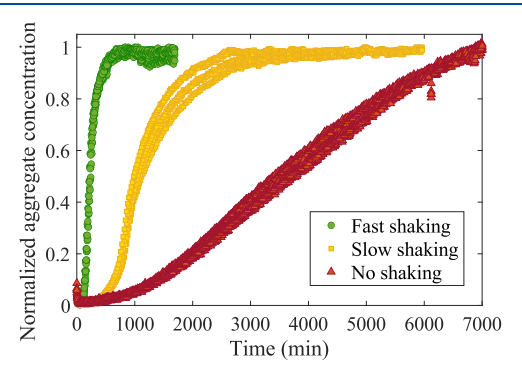


Figure 3. Comparison of the normalized aggregate mass concentration across three different agitation rates with an initial Sup35NM monomer concentration of 10 μ M. Each curve illustrates five replicates of the same experiment. Fast shaking (\bullet), slow shaking (\blacksquare), and no shaking (\blacktriangle).

monomer, without agitation, with slow agitation, and with fast agitation. Table 1 shows the bounds on the parameter values.

Fitting of Sup35NM Aggregation Curves. In the protocol established by Meisl et al., 18 the first step in determining the relevant phenomena for amyloid peptide aggregation is to plot the time to reach half the maximum fluorescence, t_{50} , versus the initial monomer concentration, m_0 , on logarithmic axes. 18 The slope, γ , and the curvature of this plot, shown in Figure 4, inform which processes may be present. Accordingly, the lack of curvature and $\gamma \approx 0.5$ indicate that primary nucleation, secondary nucleation, and fragmentation may all be significant. At the high initial monomer concentrations, there is some deviation from linearity, particularly pronounced for fast shaking; these data are excluded from the linear fitting as the shape of the aggregation curve is different from those experiments in the range of 0.25 $-15 \mu M$. Figure S1 in the Supporting Information illustrates the difference in shape with a short discussion regarding potential causes, the simplest being increased turbidity.

Using the relevant phenomena as determined by $\gamma \approx 0.5$ and defined in eqs 7–9, the PBM and accompanying kinetic parameters were fit to the aggregation time courses for initial monomer concentrations between 0.25 and 15 μ M simultaneously. Figure 4 shows the result of the initial fitting for the fast-shaking data set. The results are satisfactory, with some discrepancies at extremes of concentration and time, but an overall very good fit is obtained (Figure S2 shows the residuals for each curve and that the model deviation is between -15% and +10% for all experiments) (Figure 5).

In searching for a global optimum, it was found that different initial guesses for the parameters yielded two significantly different yet equally good solutions. The parameter fittings reflect a secondary nucleation-dominated and fragmentation-dominated solution. Both solutions give the same aggregation versus time curve, even across 2 orders of magnitude of the initial monomer concentration. However, examining the fibril length distribution lends tremendous insight into how the two solutions could be differentiated experimentally. Figure 6 shows the fibril size distribution and the origin of each fibril (primary nucleation, secondary nucleation, or fragmentation) at the end of a 10 μ M Sup35NM aggregation experiment based on both solutions. The two length distributions are very

Table 1. Bounds on Parameters in the Constrained Optimization of eq 7

parameter	$k_{\rm E}~({\rm min})^{-1}$	$n_{ m E}$	$k_{\mathrm{N1}}~(\mathrm{min})^{-1}$	n_1	$k_{ m N2}~({ m min})^{-1}$	n_2	$n_{ m m}$	$k_{\mathrm{F}}~(\mathrm{min})^{-1}$
lower bound	0	0	0	0	0	0	0	0
upper bound	1.0×10^{-3}	2	1.0×10^{-1}	2	1.0×10^{-1}	2	2	1.0×10^{-1}

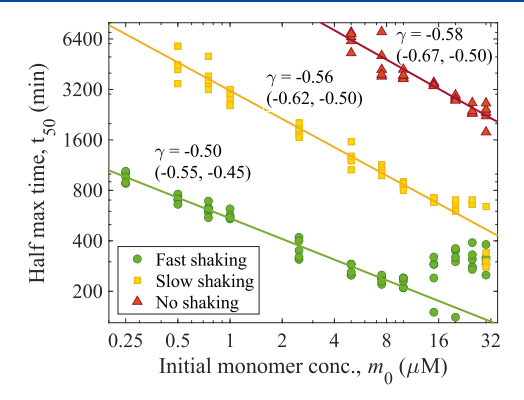


Figure 4. For each agitation condition, the time required for the system to reach half its maximum fluorescence value, t_{50} , is plotted against the initial monomer concentration, m_0 , on logarithmic axes. Fast shaking (\blacksquare), slow shaking (\blacksquare), and no shaking (\blacktriangle). The values of γ are labeled along with their 95% confidence intervals.

different, and although a technique to determine the process by which a fibril originated would be experimentally laborious, just measuring a rough size distribution would immediately indicate which parameter set is reflective of the true aggregation process.

When secondary nucleation is dominant, the aggregate size distribution is bimodal, with a population of long fibrils originating from primary nucleation and a smaller population of shorter fibrils born from secondary nucleation. Modeling the fibril size density over time indicates that an initial burst of nucleation is followed by rapid growth at high supersaturation, followed by secondary nucleation which is favored with lower supersaturation and greater aggregate mass concentration. The secondary nuclei only exist after most of the supersaturation has been consumed and therefore do not grow to be very long. The parameter values resulting from the secondary nucleation-

dominated solution are given in Table 2. In the case of no agitation, primary nucleation appears to be the only significant mechanism for the birth of new fibrils, an expected result considering both secondary nucleation and fragmentation have been correlated to agitation power.^{36,37}

When fragmentation is dominant, the aggregate size distribution is shifted toward shorter fibrils, an unsurprising result considering that approximately half of all fibrils were formed by breaking a larger fibril in half. The distribution is unimodal, and following the distribution over time shows that the large fibrils originating from the initial burst of primary nucleation (seen in the secondary nucleation-dominant distribution) are heavily fragmented by the end of the experiment. Although assumptions were made to simplify fragmentation modeling, stark differences in fibril-size distribution would exist irrespective of the fragmentation probability and fragmentation kernel used. Section 3 of the Supporting Information discusses more complex fragmentation models and contains simulation results from more aggregation experiments, and these models demonstrate how the total aggregate mass versus time is not sufficient to determine aggregation kinetics. The parameter values resulting from the fragmentation-dominated solution are given in Table 3. In reality, both secondary nucleation and fragmentation probably occur to some extent, but it is not unreasonable to assume that one is far more important than the other.

These differences highlight the need for additional orthogonal observations of amyloid fibril formation, with a focus on size distribution of aggregates, especially size distribution over time. Considerable progress has been made modeling and fitting amyloid aggregation, especially using large concentration ranges to probe effects that may dominate at some concentrations but be insignificant at others. 19,38,39 Several potential tools could give detailed length distribution information, such as dynamic light scattering (DLS), laser

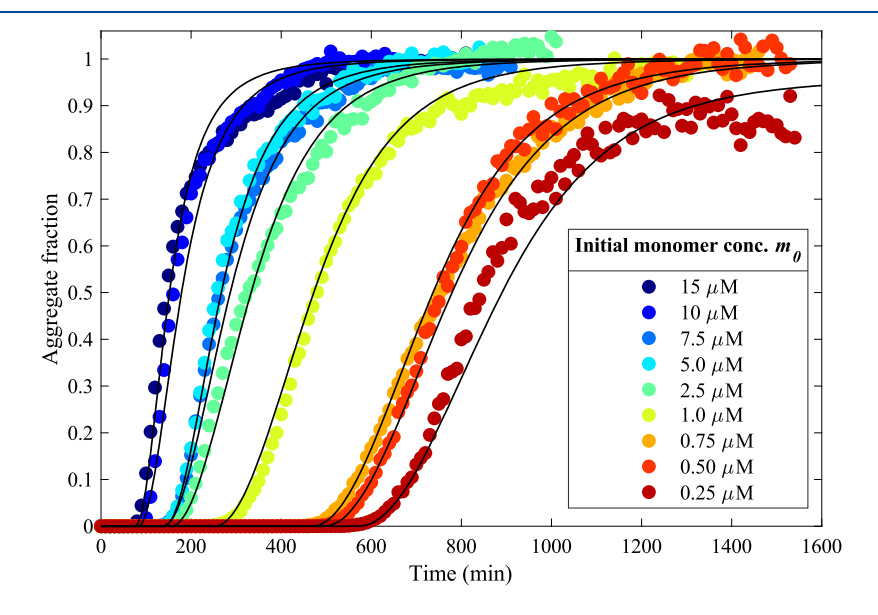
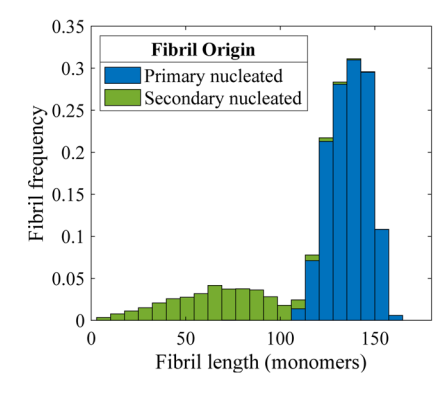


Figure 5. Fit of the PBM to all fast-shaking data for $m_0 \le 15 \ \mu\text{M}$.



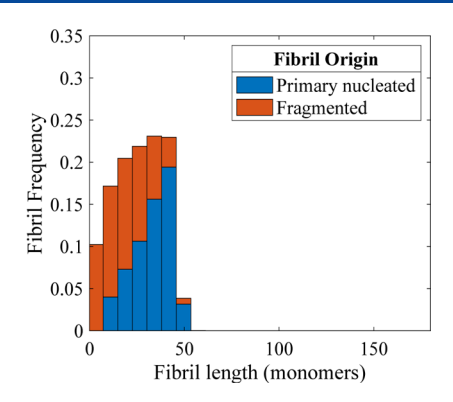


Figure 6. Two size distributions that are consistent with the aggregation kinetics measured with ThT fluorescence. The distributions are length-weighted and from the fast-shaking fits with different dominant secondary fibril formation mechanisms, the blue area represents fibrils originating from primary nucleation, the green area represents those originating from secondary nucleation (only significant on the left), and the red area represents those originating from fragmentation (only significant on the right). Both distributions represent the 10 μ M initial monomer concentration experiment but fit to the entire initial concentration span.

Table 2. Summary of Parameter Values for Secondary Nucleation-Dominated Solution

parameter	$k_{\rm E}~({ m min})^{-1}$	n_{E}	$k_{ m N1}~({ m min})^{-1}$	n_1	$k_{ m N2}~({ m min})^{-1}$	n_2	$n_{ m m}$
fast agitation	1.5×10^{-5}	0.99	1.05×10^{-2}	0.88	7.6×10^{-6}	0.50	0.34
slow agitation	6.6×10^{-6}	0.97	1.00×10^{-4}	0.72	5.2×10^{-7}	0.44	0.32
no agitation	9.2×10^{-6}	0.99	9.5×10^{-6}	0.87	ns	ns	ns

"ns" stands for "not significant".

Table 3. Summary of Parameter Values for Fragmentation-Dominated Solution a

parameter	$k_{\rm E}~({\rm min})^{-1}$	$n_{\rm E}$	$k_{\rm N1}~({\rm min})^{-1}$	n_1	$k_{\mathrm{F}}~(\mathrm{min})^{-1}$		
Fast	1.2×10^{-4}	1.0	2.2×10^{-3}	1.0	8.2×10^{-5}		
Slow	3.0×10^{-6}	1.07	3.2×10^{-4}	1.0	5.8×10^{-5}		
no agitation	9.2×10^{-6}	0.99	9.5×10^{-6}	0.87	ns		
"ns" stands for "not significant".							

diffraction, and analytical ultracentrifugation (AUC); the review of ThT fluorescence by Malmos et al. describes several orthogonal techniques to complement fluorescence time courses.²⁸

As is demonstrated in Figure 6, only a single fibril length distribution from an experiment is needed to determine all the mechanisms of new fibril formation. After observing the aggregation with ThT fluorescence, the length distribution of the fully aggregated sample can be measured and the mechanisms of aggregation are discovered with significantly more confidence than ThT fluorescence alone. Alternatively, the length distribution can be measured at many time points and used without the ThT fluorescence measurement of the total aggregate concentration. Equation 12 should be used to fit the combined ThT fluorescence and size distribution data

$$\min_{\theta} \sum_{i} \left(\frac{1}{m_{0,i}^{2}} \sum_{t}^{t_{i}} (M_{i,t} - a_{i,t})^{2} + w_{i} \sum_{t}^{t_{1}} \left[\frac{1}{M_{i,t}^{2}} \sum_{l} (A_{i,t,l} L^{p-1} - y_{i,t,l})^{2} \right] \right)$$
(12)

where i indexes the individual experiments, $t_{\rm f}$ indexes the fluorescence measurement time points, $t_{\rm l}$ indexes the fibril length distribution measurement time points, l indexes the bins of a fibril length distribution histogram reported by the size measurement device, y is the experimentally measured

population of fibrils of a certain length, w is a weighting factor to compare fluorescence and length distribution errors, L is the histogram bin center, and p is a weighting based on the fibril length distribution measurement technique. For absorption and laser diffraction, p=3 as the distribution is volume weighted and for backscattering techniques such as focused-beam reflectance measurement, p=2 as the probes see an effective area, ⁴⁰ for counting techniques that measure every fibril, p=1. The value of p for AUC depends on the method of particle detection.

Fitting of Sup35NM Fibril Length Distributions. To demonstrate how size distributions can be used with ThT fluorescence curves, data from a previous study in which a Sup35NM fibril length distribution and ThT fluorescence time course were measured at 10 μ M initial monomer concentration were reexamined. Using this single concentration point, eq 12 was minimized with p = 1 as atomic force microscopy, the technique used to collect the length distribution, counts each fibril. A conversion of 4.0 nm per monomer was used, estimated from the molecular weight of Sup35NM (28.5 kDa). It was found that fragmentation is more significant than secondary nucleation, at least at 10 µM initial monomer concentration, for Sup35NM. Figure 7 shows the experimental size distribution (bars) with the fit fibril length distribution and the best fitting length distribution when fragmentation was suppressed (k_F set to 0). The fragmentation-suppressed distribution is too narrow and does not capture the significant population of small aggregates. Regardless of constraints, neither model predicts the experimentally observed tail toward longer fibrils; however, the few observed fibrils with lengths greater than 400 nm could represent agglomerates, which were not considered here (previous studies have found fibrils agglomerated as bundles of ordered helices¹). To determine definitively the mechanism of Sup35NM aggregation, one would need size distributions sampled from several initial monomer concentrations. These measurements are beyond the

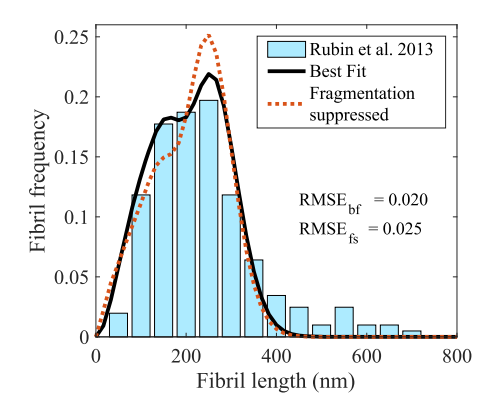


Figure 7. Experimental size distribution (bars) with the model best fit (solid black curve) and the model with fragmentation suppressed (red dashed curve). Data reproduced from Rubin et al. 2013^{1} for $10~\mu M$ Sup35NM in pH 7.4 PBS with 0.2 M sodium chloride under the fast-shaking condition.

scope of this study, but based on the preliminary results here, fragmentation may be more significant than secondary nucleation in Sup35NM, while primary nucleation and elongation also contribute considerably to the overall shape of the size distribution.

It should be noted that the data in Figure 7 reflect one specific concentration and particular experimental conditions. Further experiments are needed to determine if secondary nucleation or fragmentation plays a crucial role in defining kinetic parameters of Sup35 aggregation *in vitro* more generally. *In vivo*, Sup35 aggregates are known to be efficiently fragmented by the chaperone machinery that may shift balance toward fragmentation. The analysis of Figure 7 suggests that, at least under some solution conditions in (obviously chaperone-free) *in vitro* experiments, fragmentation is favored as well.

CONCLUSIONS

In this study, a detailed PBM for amyloid fibrillation has been developed with a purpose to enable future experiments capable of monitoring fibril length distributions to more accurately characterize the kinetics and mechanisms underlying fibril formation. Sup35NM was used as a case study to demonstrate how, with ThT aggregation measurements alone, it is not possible to definitively determine which phenomena are responsible for all aspects of amyloid aggregation. Simulation showed that different combinations of fragmentation and secondary nucleation can produce the same total aggregate mass time course, even across nearly 2 orders of magnitude in the initial monomer concentration. However, the combination of the ThT data with the aggregate size distribution data, obtained by using microscopy measurements in our previous paper enabled us to determine that fragmentation is more important than secondary nucleation in vitro at the particular concentration of monomers that was employed in that study. Previous studies have relied entirely on ThT fluorescence to draw conclusions about the impacts of different aggregation mechanisms, a method that can suffer from inherent ambiguities as this study has shown. The approach developed here can resolve such ambiguities and also benefits from directly solving a system of ordinary differential equations as opposed to fitting an approximate analytical solution. Because a shorter average length of fibrils has been related to increases in cytotoxicity, 42 insights into the evolution of amyloid fibril

length distributions as provided by the proposed method could benefit future treatments for amyloid diseases.

ASSOCIATED CONTENT

Supporting Information

The Supporting Information is available free of charge at https://pubs.acs.org/doi/10.1021/acs.jpcb.0c11250.

Aggregation experiments; residuals from the fast-shaking experiments; daughter length distribution probability density (eqn. S2) used in fragmentation models; result of fitting a fragmentation model to a simulated process; and simulated fibril length distributions (PDF)

AUTHOR INFORMATION

Corresponding Author

Andreas S. Bommarius — School of Chemical & Biomolecular Engineering, Georgia Institute of Technology, Atlanta, Georgia 30332, United States; School of Chemistry and Biochemistry, Georgia Institute of Technology, Atlanta, Georgia 30332, United States; orcid.org/0000-0003-4658-1675; Email: andreas.bommarius@chbe.gatech.edu

Authors

Aditi Sharma — School of Chemical & Biomolecular Engineering, Georgia Institute of Technology, Atlanta, Georgia 30332, United States

Matthew A. McDonald — School of Chemical & Biomolecular Engineering, Georgia Institute of Technology, Atlanta, Georgia 30332, United States; orcid.org/0000-0002-9444-3253

Harrison B. Rose — School of Chemical & Biomolecular Engineering, Georgia Institute of Technology, Atlanta, Georgia 30332, United States

Yury O. Chernoff — School of Biological Sciences, Georgia Institute of Technology, Atlanta, Georgia 30332, United States; Laboratory of Amyloid Biology, St. Petersburg State University, St. Petersburg 199034, Russia

Sven H. Behrens — School of Chemical & Biomolecular Engineering, Georgia Institute of Technology, Atlanta, Georgia 30332, United States; Polymer Science & Materials Chemistry, Exponent, Inc., Atlanta, Georgia 30326, United

Complete contact information is available at: https://pubs.acs.org/10.1021/acs.jpcb.0c11250

Author Contributions

A.S. and M.A.M. contributed equally. The article was written through contributions of all authors. All authors have given approval to the final version of the article.

Notes

The authors declare no competing financial interest.

ACKNOWLEDGMENTS

This work was supported by I/UCRC grant 1540017 (to A.S.B. and S.H.B.), grant 1336386 (to A.S.B. and others), and grant MCB 1817976 (to Y.O.C.) from the US National Science Foundation. The authors also gratefully acknowledge help from the Biopolymer Characterization (BPC) Core Lab of the Petit Institute of Bioengineering and Bioscience at Georgia Tech.

ABBREVIATIONS

AUC, analytical ultracentrifuge; DLS, dynamic light scattering; IPTG, β -D-1-thiogalactopyranoside; ODE, ordinary differential equation; PBM, population balance model; ThT, Thioflavin T

REFERENCES

- (1) Rubin, J.; Khosravi, H.; Bruce, K. L.; Lydon, M. E.; Behrens, S. H.; Chernoff, Y. O.; Bommarius, A. S. Ion-specific effects on prion nucleation and strain formation. *J. Biol. Chem.* **2013**, 288, 30300–30308.
- (2) Koo, E. H.; Lansbury, P. T.; Kelly, J. W. Amyloid diseases: Abnormal protein aggregation in neurodegeneration. *Proc. Natl. Acad. Sci. U.S.A.* **1999**, *96*, 9989–9990.
- (3) Sacchettini, J. C.; Kelly, J. W. Therapeutic strategies for human amyloid diseases. *Nat. Rev. Drug Discovery* **2002**, *1*, 267–275.
- (4) Stefani, M. Protein misfolding and aggregation: new examples in medicine and biology of the dark side of the protein world. *Biochim. Biophys. Acta, Mol. Basis Dis.* **2004**, *1739*, 5–25.
- (5) Chernoff, Y. O.; Uptain, S. M.; Lindquist, S. L. Analysis of prion factors in yeast. *Methods in Enzymology*; Academic Press, 2002; Vol. 351, pp 499–538.
- (6) Liebman, S. W.; Chernoff, Y. O. Prions in Yeast. *Genetics* **2012**, 191, 1041–1072.
- (7) Shorter, J.; Lindquist, S. Prions as adaptive conduits of memory and inheritance. *Nat. Rev. Genet.* **2005**, *6*, 435–450.
- (8) Serio, T. R.; Cashikar, A. G.; Kowal, A. S.; Sawicki, G. J.; Moslehi, J. J.; Serpell, L.; Arnsdorf, M. F.; Lindquist, S. L. Nucleated Conformational Conversion and the Replication of Conformational Information by a Prion Determinant. *Science* **2000**, 289, 1317–1321.
- (9) Gebauer, D.; Cölfen, H. Prenucleation clusters and non-classical nucleation. *Nano Today* **2011**, *6*, 564–584.
- (10) Arosio, P.; Knowles, T. P. J.; Linse, S. On the lag phase in amyloid fibril formation. *Phys. Chem. Chem. Phys.* **2015**, *17*, 7606–7618.
- (11) Cohen, S. I. A.; Linse, S.; Luheshi, L. M.; Hellstrand, E.; White, D. A.; Rajah, L.; Otzen, D. E.; Vendruscolo, M.; Dobson, C. M.; Knowles, T. P. J. Proliferation of amyloid-β42 aggregates occurs through a secondary nucleation mechanism. *Proc. Natl. Acad. Sci. U.S.A.* **2013**, *110*, 9758–9763.
- (12) Cohen, S. I. A.; Vendruscolo, M.; Dobson, C. M.; Knowles, T. P. J. From macroscopic measurements to microscopic mechanisms of protein aggregation. *J. Mol. Biol.* **2012**, *421*, 160–171.
- (13) Meisl, G.; Yang, X.; Hellstrand, E.; Frohm, B.; Kirkegaard, J. B.; Cohen, S. I. A.; Dobson, C. M.; Linse, S.; Knowles, T. P. J. Differences in nucleation behavior underlie the contrasting aggregation kinetics of the $A\beta$ 40 and $A\beta$ 42 peptides. *Proc. Natl. Acad. Sci. U.S.A.* **2014**, *111*, 9384–9389.
- (14) Nicoud, L.; Lazzari, S.; Balderas Barragán, D.; Morbidelli, M. Fragmentation of amyloid fibrils occurs in preferential positions depending on the environmental conditions. *J. Phys. Chem. B* **2015**, *119*, 4644–4652.
- (15) Cohen, S. I. A.; Vendruscolo, M.; Welland, M. E.; Dobson, C. M.; Terentjev, E. M.; Knowles, T. P. J. Nucleated polymerization with secondary pathways. I. Time evolution of the principal moments. *J. Chem. Phys.* **2011**, *135*, 065105.
- (16) Cohen, S. I.; Vendruscolo, M.; Dobson, C. M.; Knowles, T. P. Nucleated polymerization with secondary pathways. II. Determination of self-consistent solutions to growth processes described by non-linear master equations. *J. Chem. Phys.* **2011**, *135*, 08B611.
- (17) Cohen, S. I. A.; Vendruscolo, M.; Dobson, C. M.; Knowles, T. P. J. Nucleated polymerization with secondary pathways. III. Equilibrium behavior and oligomer populations. *J. Chem. Phys.* **2011**, *135*, 065107.
- (18) Meisl, G.; Kirkegaard, J. B.; Arosio, P.; Michaels, T. C. T.; Vendruscolo, M.; Dobson, C. M.; Linse, S.; Knowles, T. P. J. Molecular mechanisms of protein aggregation from global fitting of kinetic models. *Nat. Protoc.* **2016**, *11*, 252–272.

- (19) Meisl, G.; Michaels, T. C. T.; Linse, S.; Knowles, T. P. J. Kinetic analysis of amyloid formation. *Amyloid Proteins*; Springer, 2018; pp 181–196.
- (20) Ferrone, F. Analysis of protein aggregation kinetics. *Methods Enzymol.* 1999, 309, 256–274.
- (21) Knowles, T. P. J.; Waudby, C. A.; Devlin, G. L.; Cohen, S. I. A.; Aguzzi, A.; Vendruscolo, M.; Terentjev, E. M.; Welland, M. E.; Dobson, C. M. An Analytical Solution to the Kinetics of Breakable Filament Assembly. *Science* **2009**, *326*, 1533.
- (22) Selkoe, D. J.; Hardy, J. The amyloid hypothesis of Alzheimer's disease at 25 years. *EMBO Mol. Med.* **2016**, *8*, 595–608.
- (23) Yeh, V.; Broering, J. M.; Romanyuk, A.; Chen, B.; Chernoff, Y. O.; Bommarius, A. S. The Hofmeister effect on amyloid formation using yeast prion protein. *Protein Sci.* **2010**, *19*, 47–56.
- (24) Sharma, A.; Behrens, S. H.; Chernoff, Y. O.; Bommarius, A. S. Modulation of the Formation of A β and Sup35NM-Based Amyloids by Complex Interplay of Specific and Nonspecific Ion Effects. *J. Phys. Chem. B* **2018**, 122, 4972–4981.
- (25) Allen, K. D.; Wegrzyn, R. D.; Chernova, T. A.; Müller, S.; Newnam, G. P.; Winslett, P. A.; Wittich, K. B.; Wilkinson, K. D.; Chernoff, Y. O. Hsp70 Chaperones as Modulators of Prion Life Cycle. *Genetics* **2005**, *169*, 1227–1242.
- (26) Naiki, H.; Higuchi, K.; Hosokawa, M.; Takeda, T. Fluorometric determination of amyloid fibrils in vitro using the fluorescent dye, thioflavine T. *Anal. Biochem.* **1989**, *177*, 244–249.
- (27) Biancalana, M.; Koide, S. Molecular mechanism of Thioflavin-T binding to amyloid fibrils. *Biochim. Biophys. Acta, Proteins Proteomics* **2010**, *1804*, 1405–1412.
- (28) Malmos, K. G.; Blancas-Mejia, L. M.; Weber, B.; Buchner, J.; Ramirez-Alvarado, M.; Naiki, H.; Otzen, D. ThT 101: a primer on the use of thioflavin T to investigate amyloid formation. *Amyloid* **2017**, 24, 1–16.
- (29) Randolph, A. D.; Larson, M. A. Chapter 3—The Population Balance. In *Theory of Particulate Processes*; Randolph, A. D., Larson, M. A., Eds.; Academic Press, 1971; pp 41–63.
- (30) Powers, E. T.; Powers, D. L. The Kinetics of Nucleated Polymerizations at High Concentrations: Amyloid Fibril Formation Near and Above the "Supercritical Concentration". *Biophys. J.* **2006**, *91*, 122–132.
- (31) Thacker, D.; Sanagavarapu, K.; Frohm, B.; Meisl, G.; Knowles, T. P. J.; Linse, S. The role of fibril structure and surface hydrophobicity in secondary nucleation of amyloid fibrils. *Proc. Natl. Acad. Sci. U.S.A.* **2020**, 117, 25272.
- (32) Li, H.; Yang, B.-S. Model evaluation of particle breakage facilitated process intensification for Mixed-Suspension-Mixed-Product-Removal (MSMPR) crystallization. *Chem. Eng. Sci.* **2019**, 207, 1175–1186.
- (33) Borsos, Á.; Lakatos, B. G. Investigation and simulation of crystallization of high aspect ratio crystals with fragmentation. *Chem. Eng. Res. Des.* **2014**, 92, 1133–1141.
- (34) Salvatori, F.; Mazzotti, M. Experimental Characterization and Mathematical Modeling of Breakage of Needle-like Crystals in a Continuous Rotor-Stator Wet Mill. *Cryst. Growth Des.* **2018**, *18*, 5957–5972.
- (35) Grof, Z.; Schoellhammer, C. M.; Rajniak, P.; Štěpánek, F. Computational and experimental investigation of needle-shaped crystal breakage. *Int. J. Pharm.* **2011**, *407*, 12–20.
- (36) Ploß, R.; Mersmann, A. A new model of the effect of stirring intensity on the rate of secondary nucleation. *Chem. Eng. Technol.* **1989**, *12*, 137–146.
- (37) Xue, W.-F.; Hellewell, A. L.; Hewitt, E. W.; Radford, S. E. Fibril fragmentation in amyloid assembly and cytotoxicity: when size matters. *Prion* **2010**, *4*, 20–25.
- (38) Iadanza, M. G.; Jackson, M. P.; Hewitt, E. W.; Ranson, N. A.; Radford, S. E. A new era for understanding amyloid structures and disease. *Nat. Rev. Mol. Cell Biol.* **2018**, *19*, 755–773.
- (39) Michaels, T. C. T.; Šarić, A.; Habchi, J.; Chia, S.; Meisl, G.; Vendruscolo, M.; Dobson, C. M.; Knowles, T. P. J. Chemical Kinetics for Bridging Molecular Mechanisms and Macroscopic Measurements

- of Amyloid Fibril Formation. Annu. Rev. Phys. Chem. 2018, 69, 273-298
- (40) Heath, A. R.; Fawell, P. D.; Bahri, P. A.; Swift, J. D. Estimating Average Particle Size by Focused Beam Reflectance Measurement (FBRM). *Part. Part. Syst. Charact.* **2002**, *19*, 84–95.
- (41) Chernova, T. A.; Wilkinson, K. D.; Chernoff, Y. O. Prions, Chaperones, and Proteostasis in Yeast. *Cold Spring Harbor Perspect. Biol.* **2017**, *9*, a023663.
- (42) Xue, W.-F.; Hellewell, A. L.; Gosal, W. S.; Homans, S. W.; Hewitt, E. W.; Radford, S. E. Fibril fragmentation enhances amyloid cytotoxicity. *J. Biol. Chem.* **2009**, 284, 34272–34282.